

See discussions, stats, and author profiles for this publication at: <https://www.researchgate.net/publication/347847263>

A study of the effect of serration shape and flexibility on trailing edge noise

Article in Physics of Fluids · December 2020

DOI: 10.1063/5.0032774

CITATIONS
20

READS
354

5 authors, including:



Siyang Zhong
The Hong Kong University of Science and Technology

75 PUBLICATIONS 360 CITATIONS

[SEE PROFILE](#)



Yi Fang
The Hong Kong University of Science and Technology

40 PUBLICATIONS 385 CITATIONS

[SEE PROFILE](#)



Xin Zhang
Cardiff University

229 PUBLICATIONS 3,609 CITATIONS

[SEE PROFILE](#)

Some of the authors of this publication are also working on these related projects:



airfoil leading edge noise in transonic flow [View project](#)



Sound projection methods in turbulent flow [View project](#)

A study of the effect of serration shape and flexibility on trailing edge noise EP

Cite as: Phys. Fluids 32, 127114 (2020); <https://doi.org/10.1063/5.0032774>

Submitted: 10 October 2020 . Accepted: 30 November 2020 . Published Online: 22 December 2020

 Peng Zhou (周朋),  Qian Liu (刘倩),  Siyang Zhong (钟思阳),  Yi Fang (方亦), and  Xin Zhang (张欣)

COLLECTIONS

 This paper was selected as an Editor's Pick



[View Online](#)

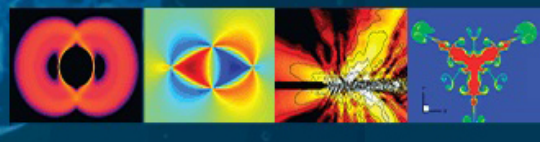


[Export Citation](#)



[CrossMark](#)

Physics of Fluids GALLERY OF COVERS



A study of the effect of serration shape and flexibility on trailing edge noise

Cite as: Phys. Fluids 32, 127114 (2020); doi: 10.1063/5.0032774

Submitted: 10 October 2020 • Accepted: 30 November 2020 •

Published Online: 22 December 2020



View Online



Export Citation



CrossMark

Peng Zhou (周朋),  Qian Liu (刘倩),  Siyang Zhong (钟思阳),  Yi Fang (方亦),  and Xin Zhang (张欣)^a 

AFFILIATIONS

Department of Mechanical and Aerospace Engineering, The Hong Kong University of Science and Technology, Clear Water Bay, Hong Kong, China

^aAuthor to whom correspondence should be addressed: aexzhang@ust.hk

ABSTRACT

In this study, we investigated the performance of flexible trailing edge serrations of various shapes for airfoil self-noise reduction through anechoic wind tunnel experiments. A flat plate model was tested at zero angle of attack. The chord-based Reynolds number was between 1.6×10^5 and 4×10^5 . The boundary layers were fully tripped near the leading edge. Add-on type trailing edge serrations were cut from flexible polyethylene terephthalate sheets. It is observed that compared with rigid serrations, flexible serrations can achieve an additional broadband noise reduction up to 2 dB–3 dB at high frequencies, and the effect also depends on the geometry of the serrations. Complementary deformation measurement and aerodynamic force measurement show that flexible serrations can align better with the flow and are expected to reduce the crossflow intensity near the serration roots, which has been related to the extraneous high-frequency noise generated by serrations in previous studies. An inviscid model is proposed to predict the wake structure and the loadings for serrations of various shapes. Although the model over-predicts the crossflow speed due to the omission of the viscous effect, the relative intensity corresponding to different serration geometry is consistent with experimental observations. Last, we show that the recent analytical noise prediction model [B. Lyu and L. J. Ayton, “Rapid noise prediction models for serrated leading and trailing edges,” *J. Sound Vib.* **469**, 115136 (2020)] for a serrated trailing edge still significantly overpredicts the noise reduction capacity by serrations and does not reveal the role of serration shape properly. This indicates the necessity to include the non-frozen turbulent properties near serrations in the future prediction models.

Published under license by AIP Publishing. <https://doi.org/10.1063/5.0032774>

I. INTRODUCTION

Trailing edge noise is an important noise source for many industrial applications, such as the airframe noise for aircraft in clean configuration,² wind turbine noise,³ and aeroengine fan noise. Depending on the nature of the flow past the trailing edge, the noise can be either tonal or broadband. Tonal noise can appear when the boundary layer before the trailing edge is laminar (laminar boundary layer-vortex shedding noise), or when the trailing edge is blunt (trailing edge bluntness-vortex shedding noise).⁴ If the boundary layer is turbulent, and the trailing edge is sufficiently sharp, then the trailing edge noise is broadband (turbulent boundary layer-trailing edge noise). The major mechanism of broadband trailing edge noise is edge scattering, which converts the flow energy in the turbulent boundary layer to the out-radiating acoustic energy.^{5,6}

Inspired by the fringe structure of owls' feather, researchers have developed trailing edge serrations as a special method to

mitigate trailing edge noise. Howe⁷ did the first theoretical study to demonstrate the effect of the serrated trailing edge on the trailing edge scattering process and found a great noise reduction potential by serrations. His analytical study showed that serrations with a wavelength of λ and a root-to-tip distance of $2h$ could achieve more than $10 \log_{10}[1 + (4h/\lambda)^2]$ dB noise reduction compared with the unserrated counterpart, in the high-frequency limit. Lyu, Azarpayvand, and Sinayoko⁸ and Ayton⁹ have developed semi-analytical models that can better estimate the noise reduction by serrations.

Meanwhile, a variety of experimental studies have been conducted to study the essential parameters of trailing edge serrations.^{3,10–14} Oerlemans *et al.*³ successfully applied serrated structures to a full-scale wind turbine blade and achieved a 3.2 dB overall noise reduction. Gruber¹⁰ conducted a comprehensive experimental study on the serration parameters and suggested that, to achieve noise reduction, the serration length should satisfy the condition

$2h \gtrsim \delta$, where δ is the boundary layer thickness. Moreau and Doolan¹¹ studied the effect of serrations at a chord-based Reynolds number between 8×10^4 and 4.2×10^5 and found that the serrations are also effective in eliminating vortex-shedding tones by up to 13 dB. Several variations of the serrat structures were also proposed in the literature, for example, non-flat type serrations,¹⁵ poroserrations,¹⁶ combed-sawtooth (ST) serrations,¹⁷ and iron-shaped (IR) serrations.¹⁸

In experimental studies, the prominent drawback of serrations is the unpreferred noise increment above a crossover frequency,^{3,14} which is not captured by theoretical models.^{7,8} The large deviation from Howe's theory at high frequencies was attributed to the failure of Taylor's frozen turbulence assumptions.^{8,19} Gruber¹⁰ attributed the high-frequency noise increment to the increased turbulence intensity between serrat teeth. The noise increment at high frequencies is greater if there is a misalignment between the serrat and the undisturbed wake flow,²⁰ and more significantly when serrations have flap angles.^{12–14} Avallone, Pröbsting, and Ragni²¹ suspected that the crossflow increased the high-frequency noise by continuously pushing the high moment fluid toward the serrat surface. León *et al.*¹⁴ conducted particle image velocimetry (PIV) measurements of a serrated airfoil and observed an increased wall-normal velocity fluctuation at the pressure side edge of the serrations, at the crossover frequency, which is believed to be linked with the origin for the noise increment.

In nature, the lifting surfaces of birds are typically composed of non-rigid feathers. For example, it is well-known that some owls have soft fringes at the trailing edge of their wings.²² However, up to now, the flexibility of the trailing edge serrations has not been considered a critical parameter in the design process, and most serrations in the experimental studies were rigid. The effect of trailing edge compliance on trailing edge noise has been addressed in the literature. Crighton and Leppington²³ did a theoretical analysis and found that, for a sufficiently compliant trailing edge under heavy fluid loading, the emitted acoustic power depends on the sixth-power of flow velocity, in contrast to the well-known fifth-power dependence of a rigid trailing edge.⁵ Jaworski and Peake²⁴ further investigated the separated and combined effects of trailing edge flexibility and porosity on edge scattering. However, in these studies, the effect of the compliant wall was only considered in the framework of the edge scattering process and no fluid–structure interaction effect was considered. There were a few experimental studies of airfoil self-noise using a flexible configuration in the trailing edge region. Herr and Dobrzynski²⁵ and Herr²⁶ used flexible trailing edge brushes to achieve a broadband trailing edge noise reduction by 2 dB–10 dB and found that the flexibility of the brushes was beneficial for noise reduction. Finez *et al.*²⁷ also used flexible trailing edge brushes but only achieved 3 dB broadband noise reduction. Although the flexibility of the add-on structure was found to be beneficial in these studies, the exact role of flexibility was unclear. Recently, Talboys, Geyer, and Brücker²⁸ used flexible self-oscillating trailing edge flaps to reduce the laminar boundary layer–trailing edge noise. They attributed the effect to the disturbance of T-S instabilities in the laminar boundary layer by the oscillation elements. Nevertheless, the role of the flexibility of trailing edge serrations in the context of turbulent boundary layer–trailing edge noise has not been widely studied.

In this work, the effect of the flexibility of trailing edge serrations on trailing edge noise is investigated experimentally. Various serrat geometries were included in this experimental campaign to provide a more generic picture. Deformation measurement and aerodynamic force measurement were also conducted to enable a better understanding of the noise reduction mechanisms. This paper is organized as follows: Sec. II briefly introduces the experimental setup; Sec. III presents the experimental results; Sec. IV provides theoretical analysis related to the observed phenomenon; and, last, Sec. V provides the conclusion.

II. EXPERIMENTAL SETUP

A. Anechoic wind tunnel facility and the test model

The trailing edge noise measurements of a flat plate model were conducted in an anechoic wind tunnel, Ultra-quiet Noise Injection Test and Evaluation Device (UNITED),^{29,30} at The Hong Kong University of Science and Technology. Figure 1 gives the layout of the experiment. An open-jet test section was used in this study. The nozzle of the wind tunnel has a square cross section with a side length of 0.4 m. The flow speed can vary from 10 m/s to 70 m/s, and the inflow turbulence intensity is lower than 0.32% for the whole speed range. The test section is enclosed by an anechoic chamber with a cut-off frequency of about 200 Hz. Dimensions of the chamber are 3.3 (L) × 3.1 (W) × 2.0 m³ (H). A microphone array and a balance set were used to measure the trailing edge noise and aerodynamic loading, respectively. In addition, a 2D laser profiler was used to capture the shape of the serrations that are attached to the trailing edge of the test model. The functions of the equipment will be detailed in Secs. II C–II E.

A flat plate model is used in this experimental study. The model has a chord of 150 mm, a span of 400 mm, and a thickness of 6 mm. The leading edge is a 4:1 semi-ellipse, and the trailing edge is symmetrical with 12° contraction angle. Serrated trip strips with 0.3 mm thickness were applied to both sides of the model, covering 13%–20% portion of the chord, to ensure turbulent boundary layers at the trailing edge. The trailing edge thickness is less than 0.2 mm. The angle of attack of the flat plate model was set at 0°

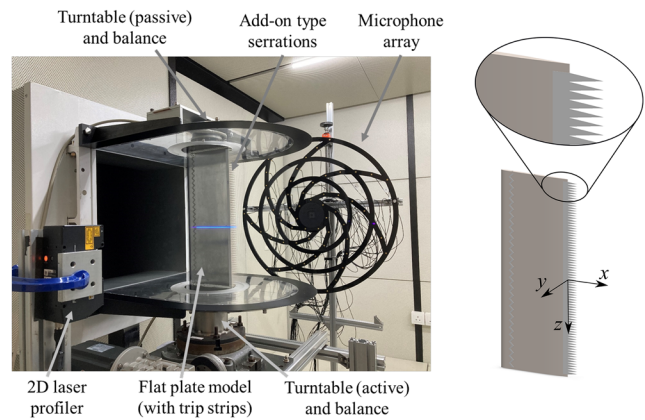


FIG. 1. Experimental setup in this study and a zoomed-in view of the add-on trailing edge serrat.

in the experiment. The freestream velocity U_0 in this experiment ranges between 16 m/s and 40 m/s, corresponding to a chord-based Reynolds number between 1.6×10^5 and 4×10^5 .

The coordinate system in this study is shown in Fig. 1: the origin is located at the center of the trailing edge of the baseline model (i.e., without serrations); the z -axis represents the spanwise direction and is aligned with the trailing edge; the x -axis is aligned with the chord of the flat plate model; and the y -axis is perpendicular to the xz -plane.

B. Flexible serrations

Four different serrat geometry were investigated in this study, as shown in Fig. 2. The sawtooth geometry consists of straight edges connecting the roots and tips. The iron shaped geometry consists of circular arcs that are tangent to the chord at the serrat roots. The chopped root (CR) geometry has a gap at the serrat root, which has a width of 20% of the serrat wavelength. The chopped peak (CP) geometry has a flat tip that has a width of 20% of the serrat wavelength. For all serrations, the root-to-tip distance is $2h = 20$ mm, which is approximately equal to four times the boundary layer thickness at 20 m/s (based on XFOIL³¹ computations). The serrat wavelength is $\lambda = 5$ mm, leading to $h/\lambda = 2$. The geometrical settings fulfill the basic requirement to achieve a good noise reduction performance as indicated in previous studies.^{8,10}

The serrations were laser cut from Polyethylene Terephthalate (PET) sheets, with Young's modulus of 2.4 GPa. The thickness H ranges from 0.025 mm to 0.1 mm. The span of each piece of serrations was 390 mm, leaving ~5 mm empty space on both sides. This value was determined after several trials to reduce extraneous noise at the model-endplate junction. The serrations were attached to the trailing edge of the flat plate model by 0.05 mm-thick double-sided tape, such that the serrat roots are located along the original trailing edge of the airfoil model. The serrations have a 6° inherent flap angle, which is equal to half of the trailing edge contraction angle of the flat plate model. Therefore, the local flow is not perfectly aligned with the serrations. A certain extent of flow-serrat misalignment is also expected in engineering applications, for example, wind turbines, due to installation or manufacturing tolerances of serrations and the non-zero camber of the airfoil.¹⁴

C. Phased microphone array measurements

A phased microphone array, consisting of 56 1/4 in. Brüel & Kjær type 4957 microphones, as shown in Fig. 1, was used to

measure both the noise source distribution and the trailing edge noise level. The array was set parallel to the flow direction with its center aligned with the center of the airfoil trailing edge. The distance between the array and the trailing edge was 0.73 m. The microphone signals were acquired simultaneously with four 24-bit National Instrument PXIE-4497 acquisition cards, with a sampling frequency of 48 kHz and 409 600 data points per measurement and channel. A conventional beamforming (CB) method was used to calculate the source distribution within the model plane, and a source integration method was used to retrieve the noise spectra in the trailing edge region. For details of the postprocessing method, readers are referred to the study of Zhou *et al.*³²

D. 2D deformation measurement

A Keyence 2D laser profiler was used to capture the shape of the serrations along the streamwise direction. As shown in Fig. 1, a blue laser line is projected to the flat plate (or airfoil) model, and the 2D laser profiler measures the distance between the sensor head and each point on the projected laser line to generate a 2D profile. The laser line is horizontal and intersects with one of the serrat tips. The 2D profile is sufficient to describe the 3D shape of the serrations, as the major deflection (due to bending) of the serrations is in the wall-normal direction. In addition, in the experiment, no significant spanwise deflection of the serrations was observed. The repeatability and the accuracy of the measurement are 5 μm and 0.1% of the full-scale range, respectively. For each configuration, 100 consecutive measurements with a 50 Hz sampling rate were taken, and the average profile was used to calculate the deformation. A relatively low sampling rate was used here as only the mean deformation value is of interest.

E. Aerodynamic force measurement

A dual-balance setup was used to measure the aerodynamic force simultaneously with the acoustic measurement. This setup eliminates the gap on one side of the airfoil model, which typically generates strong noise that deteriorates the noise measurement results. The bottom balance is connected to a turntable that can actively control the angle of attack of the airfoil. The top balance, on the other hand, is connected to a passively rotating plate. Therefore, the system is able to measure the lift and drag forces of the airfoil at a different angle of attack and maintains good structural rigidity.

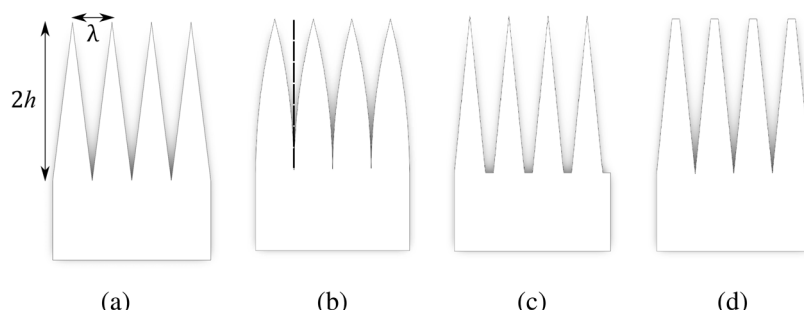


FIG. 2. Four types of serrat geometries used in this study: (a) sawtooth (ST), (b) iron-shaped (IR), (c) chopped root (CR), and (d) chopped peak (CP).

Two JR3 20E12A4-125-EF mFS balances were used in the setup. Each balance has a load of 40 N in both the X-direction and the Y-direction, which aligns with the streamwise direction and the transverse direction at a zero angle of attack. The nominal accuracy is 0.25% of the measurement range. The amplified voltage output was measured using a National Instrument PXIe-4497 card. For each measurement, the sampling frequency and duration are 2000 Hz and 10 s, respectively.

III. RESULTS AND DISCUSSIONS

A. Acoustic measurements

In this section, the aeroacoustic performance of serrations of different geometries and thicknesses is compared. Following this section, the deformation and force measurements will also be presented to give a complete picture of the phenomenon.

1. Acoustic imaging results

Before comparing the integrated sound source magnitude between different configurations, the sound maps of the baseline configuration (no serration) and representative serrated configuration (0.1-mm thick sawtooth), at 5000 Hz and at $U_0 = 20$ m/s, are presented in Fig. 3. The solid rectangle represents the flat plate model, and the dotted-dashed rectangle represents the integration region. It is evident that for both configurations, the primary sound sources are distributed along the trailing edge of the model. For the baseline case, the distribution is rather uniform along the span. For the serrated case, the sound source magnitude near the mid-span region is reduced significantly compared to the baseline. Two stronger source regions can be observed at the model-endplate junction. However, their effect on the sound source integration can be neglected at most frequencies of interest. The asymmetry of the sound map with respect to the mid-span plane is due to the slight asymmetry of the installation of serrations.

2. The effect of serration geometry on trailing edge noise

Next, the performances among different serration geometries are compared. The relatively rigid serrations ($H = 0.1$ mm) are compared first. Figure 4 shows the sound spectra of the baseline, the serrated configurations, and the background. The background noise was measured without the flat plate model, and the same integration region was used for the sound source integration. The background noise is only significant in the very-low-frequency range. From Fig. 4, it is obvious that the serration geometry has a significant effect on aeroacoustic performance. The iron-shaped (IR) serrations give slightly larger noise reduction (1 dB–2 dB) compared to the sawtooth (ST) serrations at low frequencies but have poorer performance in the high-frequency range. In particular, at $U_0 = 20$ m/s, the IR serrations even produce higher noise compared to the baseline case, at above 10 kHz. The chopped root (CR) serrations, although only having a 20% gap at the root, perform much inferior in the low-to-medium frequency range. The chopped peak (CP) serrations perform almost the same as the sawtooth serrations at low frequencies but generate slightly higher noise at high frequencies. At $U_0 = 40$ m/s, the general trends are the same, though the differences at low frequencies (2 kHz–6 kHz) are relatively larger.

Figure 5 is a scattered plot showing the amount of noise reduction by different types of serrations as a function of the boundary layer thickness-based Strouhal number $St_\delta = \delta/U_0$. Here, a negative sign in ΔSPL indicates noise reduction, and vice versa. The boundary layer thicknesses δ were acquired using XFOIL³¹ based on the baseline geometry. Below $St_\delta \lesssim 0.1$, the noise reduction appears to be close to zero, which is an artifact since the trailing edge noise is overwhelmed by the background noise. Although there is a certain amount of data scattering, generally speaking, when $St_\delta \lesssim 0.6$, the iron-shaped serrations perform best and can achieve a maximum noise reduction up to 6 dB; the sawtooth serrations and chopped peak serrations perform quite similar and can achieve a maximum noise reduction of around 4 dB–5 dB; and the chopped root

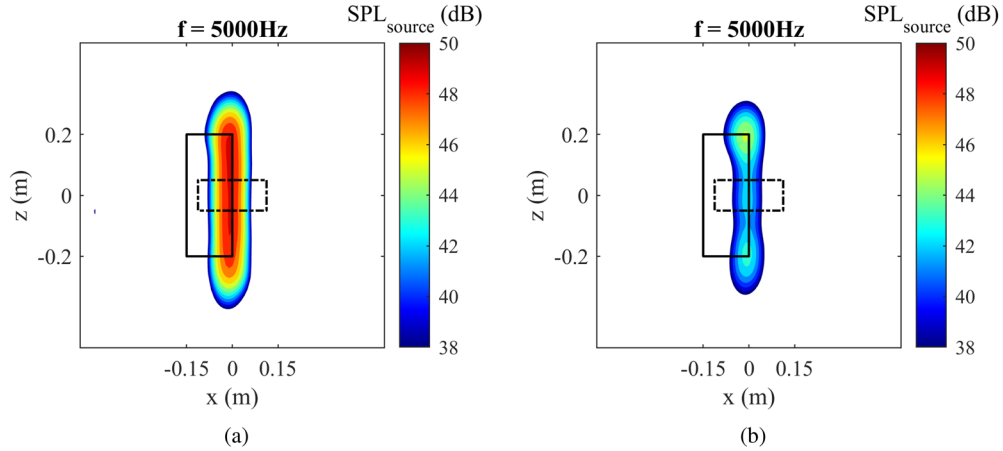


FIG. 3. Third-octave sound source maps centered at 5000 Hz and at $U_0 = 20$ m/s for (a) the baseline flat plate model and (b) the flat plate model with 0.1-mm thick sawtooth serrations at the trailing edge. The solid rectangle represents the flat plate model, and the dotted-dashed rectangle represents the integration region.

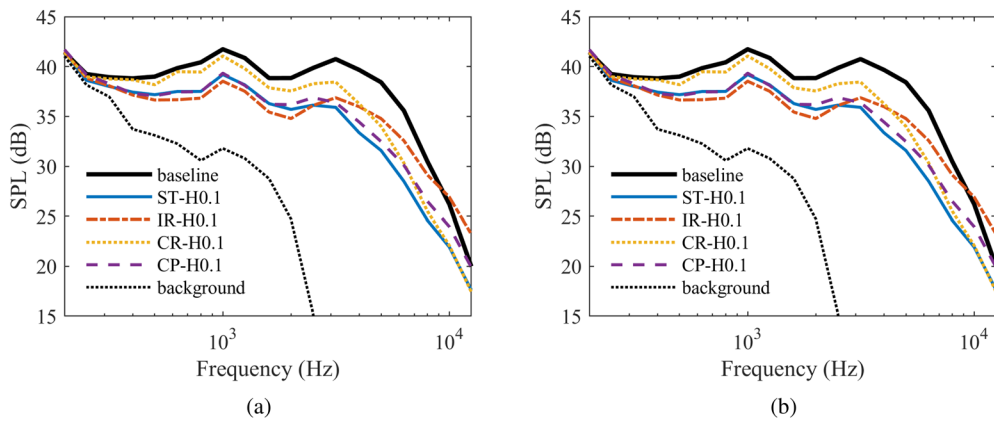


FIG. 4. Third-octave sound spectra for relatively rigid serrations at (a) $U_0 = 20$ m/s and (b) $U_0 = 40$ m/s.

serrations can only achieve a maximum noise reduction of 1 dB–2 dB in this St_δ range. On the other hand, when $St_\delta \gtrsim 0.6$, the iron-shaped serrations perform the worst and the other three perform similarly.

The additional 1 dB–2 dB benefit by the iron-shaped serrations at $St_\delta \lesssim 0.6$ is consistent with that in the numerical study by Avalone, van der Velden, and Ragni.¹⁸ In their study, a 2 dB additional noise reduction at $St_\delta < 0.75$ by iron-shaped serrations was found comparable to that by sawtooth serrations, although, in their study, a NACA 0018 airfoil was used, and the geometry of the iron-shaped serrations was slightly different from that in the current study. On the other hand, the adverse effect of the iron-shaped serrations at higher Strouhal numbers was not observed in their study, probably because the relevant frequency range is beyond the plot range shown in their results.

The vast difference in the aeroacoustic performance between the chopped root serrations and the chopped peak serrations

deserves more attention. In the analytical studies,^{9,33} under the frozen turbulence assumption, the noise reduction by serrations should remain invariant if the serrations are flipped in the streamwise direction. The large deviation between the experimental observation and the theoretical prediction is likely caused by the frozen turbulence assumption. As shown by previous numerical studies^{17,18} and an experimental study,³⁴ the low-frequency content of the wall pressure spectrum reduces rapidly along the serratation edge downstream. In this sense, at low frequencies, the shape of the serratation roots is more important than that of the serratation tips. Therefore, the chopped root serrations are expected to perform worse, as the destructive interference is not efficient in the flat region of the serratation roots. A more quantitative discussion will be given in Sec. IV B.

It is also noticed that the crossover Strouhal number, above which the serrations increase the noise level, is dependent on the serratation geometry. The crossover St_δ is ~1.8, 2.6, 3.5, and 3.6 for the IR, CP, ST, and CR serrations, respectively. Thus, the serratation geometry has a large impact on noise reduction performance at high frequencies. The deteriorated noise reduction around and above the crossover Strouhal number is typically attributed to the modified flow structure near the serrations.^{10,21}

3. The effect of serratation flexibility on trailing edge noise

Next, the effect of the flexibility of serrations is investigated. The flexibility is adjusted by the thickness of the serrations made of PET. The degree of flexibility also depends on the flow speed, as the deformation of the serratation is more prominent at a higher speed. This will be elaborated through the deformation measurement in Sec. III B. Figure 6 shows the effect of serratation thickness on trailing edge noise. It is apparent that the effect of serratation thickness (or flexibility) is highly dependent on the serratation geometry and inflow speed. For all the serrations, the flexibility effect is more prominent at higher speeds (e.g., at $U_0 = 40$ m/s). Besides, the performance of the IR serrations is relatively more sensitive to their thickness. At $U_0 = 20$ m/s, the thinner 0.05 mm serrations already give approximately an additional 2 dB noise reduction at higher frequencies.

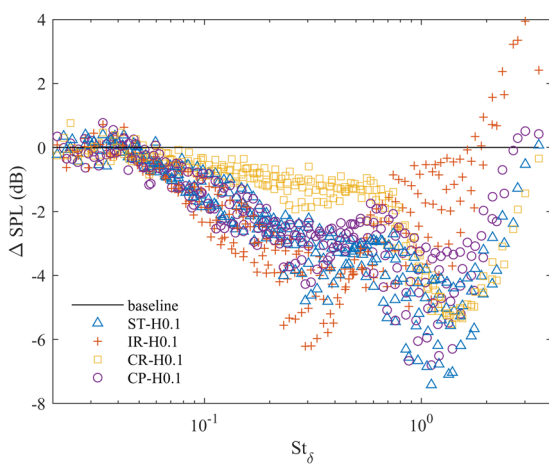


FIG. 5. Noise reduction by 0.1 mm-thick as a function of St_δ . The range of U_0 is between 16 m/s and 40 m/s. A negative ΔSPL denotes noise reduction.

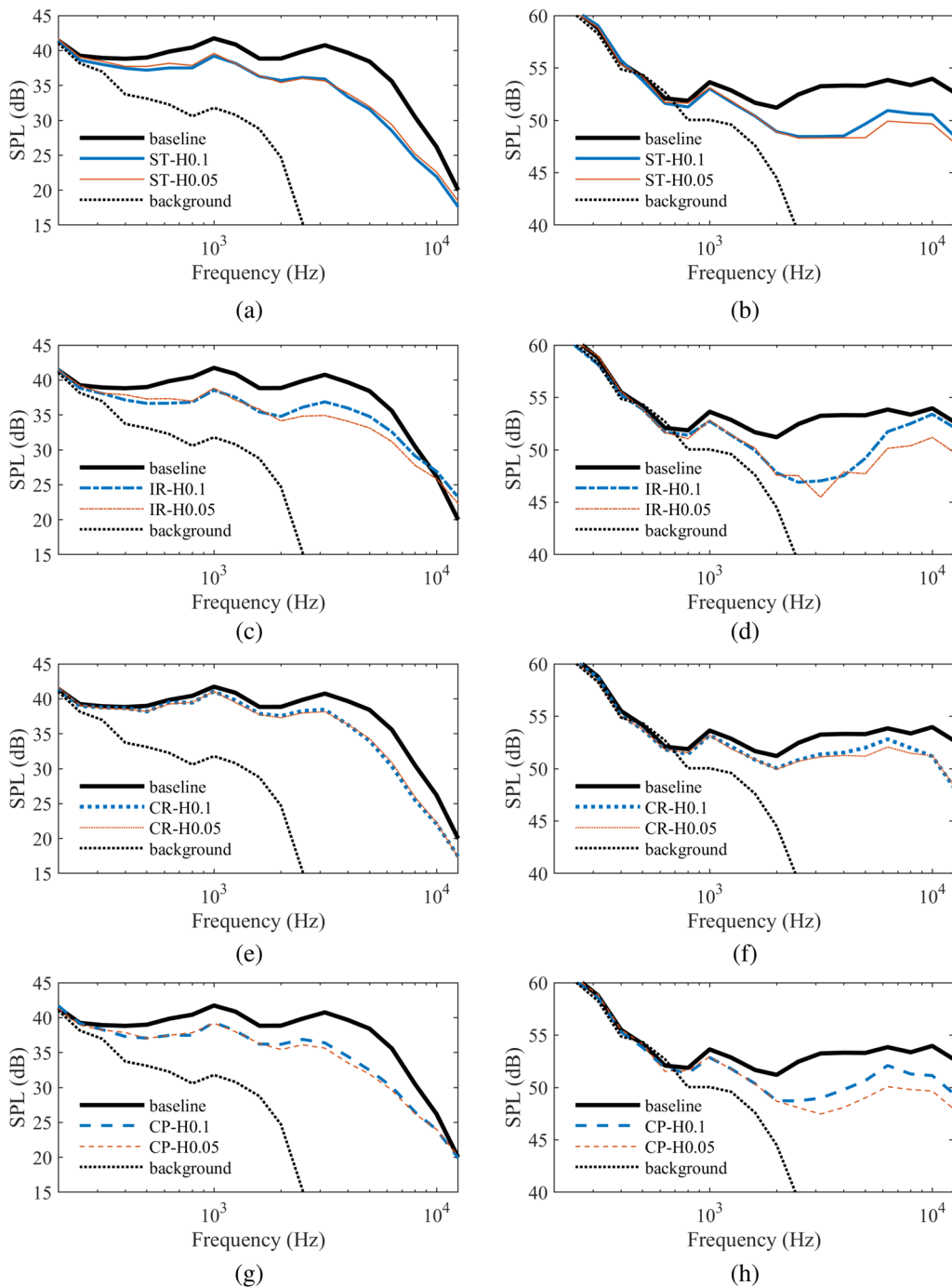


FIG. 6. Effect of serration thickness on trailing edge noise, for different serration geometries and inflow velocities. $U_0 = 20 \text{ m/s}$ for (a), (c), (e), and (g), and $U_0 = 40 \text{ m/s}$ for (b), (d), (f), and (h).

In comparison, for the ST and CR serrations, the sound spectra are almost independent of the serration thickness at $U_0 = 20 \text{ m/s}$. The dependence of the sound spectrum on the serrations' flexibility for the CP serrations is somewhere in between.

The dependence of ΔSPL on the Strouhal number St_δ is shown in Fig. 7. Although the Strouhal number may not be the most appropriate scaling, as the flexibility effect is speed-dependent, this comparison provides a general overview of the effect of flexibility on

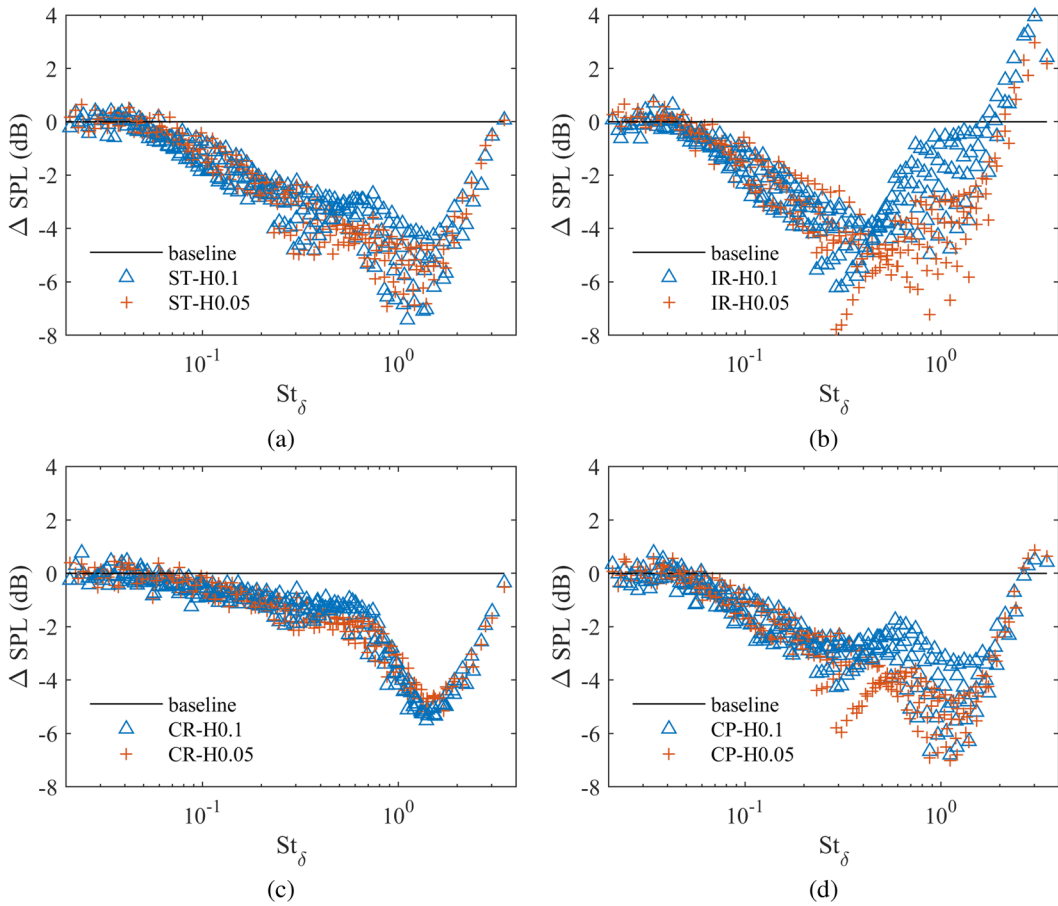


FIG. 7. Noise reduction by (a) ST serrations, (b) IR serrations, (c) CR serrations, and (d) CP serrations, with respect to the baseline as a function of St_{δ} . The range of U_0 is between 16 m/s and 40 m/s.

noise reduction. Similar to the previous conclusion, the effect of flexibility is most prominent for the iron-shaped serrations, and the relevant range is $St_{\delta} \gtrsim 0.4$. For the sawtooth serrations and chopped root serrations, the difference between H0.1 and H0.05 configurations is small, except within a narrow range where St_{δ} is close to 0.5. For the chopped peak serrations, the effective St_{δ} range is around 0.4–2. Due to the scattering of data, the above-mentioned St_{δ} is only an approximation.

The serrations with 0.025 mm thickness were also tested. However, flutter instability occurred at a relatively low flow speed, generating significant tonal and broadband noise. Many researchers have previously studied the flutter instability of a flexible plate structure.^{35,36} The structure is typically stable at low flow speeds and starts to oscillate above a critical flow speed. As shown in Fig. 8, the fluttering 0.025 mm iron-shaped serrations generate a very different noise spectrum compared to that from the more rigid counterparts.

B. Deformation measurements

In this section, the measurement results of the deformation of the serration are presented to quantify the extent of flexibility. A

quadratic curve fitting with zero intercepts is applied to fit the measured raw deformation data, as demonstrated in Fig. 9. The quality of the measured data near the tips of the serrations ($x = 20$ mm) was found to deteriorate due to optical settings, and these points were discarded for data fitting. It can be observed from Fig. 9 that the quadratic fitting can well capture the overall trend of deformation quantitatively. The deformation at the serration tip, Δy_{tip} , as illustrated in Fig. 9, is determined by extrapolating the quadratic curve. This slight extrapolation is not expected to introduce significant errors. Then, the effective reduction of the flap angle, $\Delta\delta_{flap}$, defined as

$$\Delta\delta_{flap} = \sin^{-1}\left(\frac{\Delta y_{tip}}{2h}\right),$$

is selected to quantify deformation of the flexible serrations.

Figure 10 shows the effective reduction of the flap angle in degree for different serration geometries and thicknesses. In comparison, the nominal flap angle due to installation is 6° , as stated in Sec. II B. It is apparent that the IR-H0.05 serrations have the most prominent deformation among all the configurations. The other three types of serrations have similar deformations, which are only

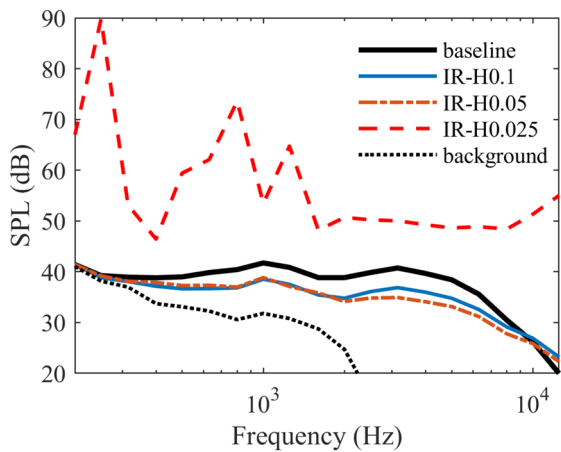


FIG. 8. Third-octave sound spectra for the iron-shaped serrations with different thicknesses at $U_0 = 20$ m/s. The 0.025 mm serrations already start to flutter at this flow speed, leading to a significantly higher noise level.

1/3 to 1/2 of the deformation of the iron-shaped serrations of the same thickness and at the same speed. At $U_0 = 20$ m/s, the difference in $\Delta\delta_{flap}$ between IR-H0.1 and IR-H0.05 is already prominent. This agrees well with the finding in Fig. 6 that, at 20 m/s flow speed, significant differences are found between the spectra of the two iron-shaped serrations with different thicknesses.

C. Aerodynamic force measurements

The measured lift and drag coefficients of different test configurations are shown in Fig. 11. The forces on the two circular end plates that are connected to the flat plate model were subtracted. The reference area used here is the planform area of the flat plate model

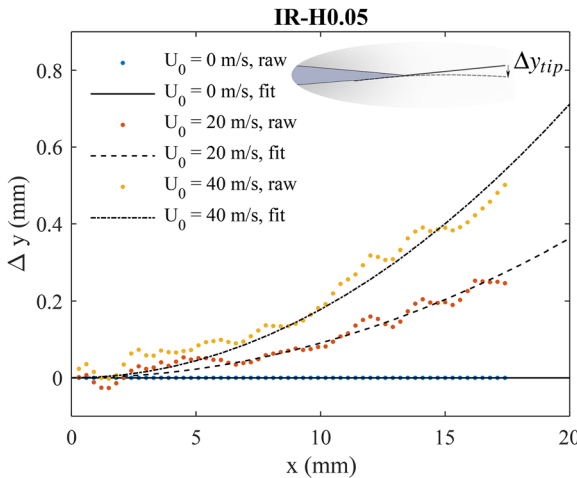


FIG. 9. Measured deformation of the 0.05 mm-thick IR serrations at various flow speeds. The dots are raw data from the laser profiler, and the solid curves are quadratic fittings. $x = 0$ is corresponding to the original trailing edge location.

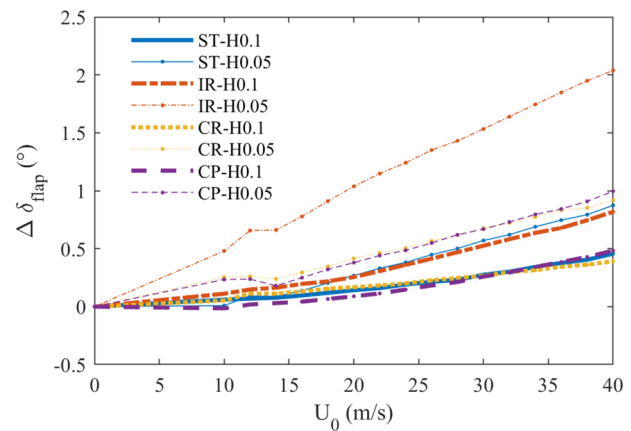


FIG. 10. Effective reduction of the flap angle $\Delta\delta_{flap}$ for different serration geometries and thicknesses.

without any serrations. The lift coefficients C_L among different serrations are clearly distinguishable. Overall, the lift coefficients are very small. In comparison, the baseline flat plate model is expected to have a C_L of 0.011 at an angle of attack of only 0.1° . In addition, according to thin-airfoil theory,³⁷ a trailing edge flap with a length equal to $h = 10$ mm and a flap angle of 6° (same with the serrations) will give a C_L of 0.221, which is significantly larger than the measured C_L of all types of serrations. Thus, it is not very effective to improve the lift coefficient by adding trailing edge serrations with flap angles.

The serrations can be put into three groups based on their C_L . The chopped root serrations result in almost the same C_L as the baseline geometry. The iron-shaped serrations lead to the largest lift coefficient. The sawtooth serrations and chopped peak serrations give very similar C_L , and the values stay in the middle. This result indicates that the geometry of the serratip roots, rather than the serratip tips, has a significant effect on the lift generation. It is expected that the wide roots of the CR configurations lead to significant flow leakage from the pressure side to the suction side, reducing the effectiveness of the flap. In comparison, the narrow root in the IR serrations may lead to less leakage. The geometry of the serratip tips is expected to have less effect on the lift, as the crossflow has partially neutralized the pressure difference across the serrations upstream.

The measured lift coefficient also varies with the flow speed U_0 . The most apparent example is IR-H0.05, whose C_L is reduced by more than 40% when U_0 changes from 20 m/s to 40 m/s. This configuration also has the largest deformation, as shown in Fig. 10. Significant reductions in C_L can also be observed for the IR-H0.1, ST-H0.05, and CP-H0.05 serrations as the speed increases. These serrations also show significant deformation at high flow speeds.

The drag coefficients of all configurations decrease at a higher flow speed, as shown in Fig. 11. All types of serrations increase the drag coefficient compared to the baseline case. However, due to the limitation of the resolution of the load cells, the drag performance of different serrations cannot be easily distinguished. Typically, the IR-H0.1 serrations lead to the largest drag penalty, and the

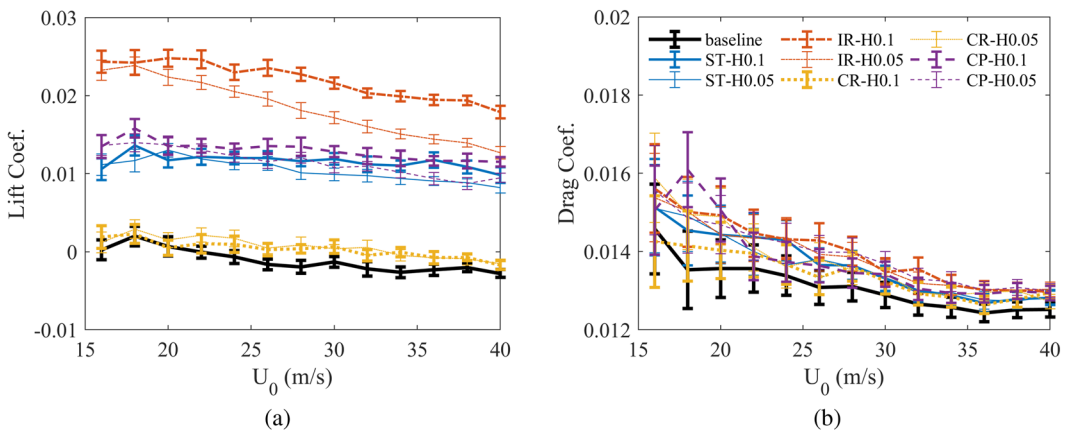


FIG. 11. (a) Lift coefficients and (b) drag coefficients of different test configurations. The range of U_0 is between 16 m/s and 40 m/s.

drag increment is around 4% compared to the baseline model at $U_0 = 40$ m/s.

D. Discussions

According to the experimental observations, we propose possible effects of serration geometry and flexibility as follows. The serration geometry is expected to directly affect the scattering efficiency of the turbulent pressure fluctuations, as shown by the theoretical analysis.⁹ Meanwhile, as inferred from the different lift coefficients corresponding to different serrated configurations, the serration geometry also affects the flow field, which can further modify the noise reduction performance, especially at high frequencies. As indicated from the deformation measurement results, the flexibility of serrations can improve flow alignment by reducing the effective flap angle, thus improving high-frequency noise reduction. The extent of flexibility depends not only on the structural rigidity of the serrations but also on the aerodynamic loading for the serrations, which depends on the flow speed and the serration geometry. In Sec. IV, we will provide theoretical analysis of the flow structure around the trailing edge serrations of different geometries and evaluate the effect of serration geometry based on the scattering theory.

IV. THEORETICAL ANALYSES

In this section, two theoretical analyses are conducted to address different aspects of trailing edge noise generation. The first one is a simplified inviscid analysis of the crossflow phenomenon, which can provide a quick qualitative evaluation of the influence of serrations on the local flow field. The second part gives the predicted noise reduction by serrations, which also highlights the effect of streamwise-varying turbulence on noise reduction. Although the two analyses are not explicitly linked in the current study, there is a strong logical connection in between, as the local three-dimensional flow can strongly affect the boundary layer characteristics and, thus, the wall pressure spectrum.

A. Simplified inviscid analysis of the crossflow phenomenon

Due to the misalignment between the serrations and the flow in this experiment, air will flow from the pressure side to the suction side through the gap area between serrations. This crossflow phenomenon has been observed in previous studies through experiments^{10,14,21} and numerical simulations.³⁸ The crossflow has also been correlated with the generation of the extraneous high-frequency noise in previous studies. Gruber¹⁰ attributed the high-frequency noise to the extra turbulence generated by the crossflow. On the other hand, Avallone, Pröbsting, and Ragni²¹ suspected that the crossflow increased the high-frequency noise by continuously pushing the high moment fluid toward the serratation surface.

Although it is more accurate to use computational fluid dynamics (CFD) to study the strength of the crossflow, it is still valuable to use a simpler inviscid approach to demonstrate how the serratation geometry affects the crossflow under various flow conditions, as the main driving force for the crossflow is the pressure difference between the pressure side and the suction side. In this work, we use a simplified potential flow method to study the effect of serratation geometry and flap angle on the intensity of the crossflow. The vortex lattice method (VLM) with semi-infinite horseshoe vortex elements is used to calculate the flow field. This method was originated from Prandtl's lifting line theory and has been widely used for preliminary wing design and optimization.³⁷ Due to the periodic structure of the serrations, a slight extension to the conventional VLM is made. The overall approach is to use the vortex line solution as the singularity element to solve the incompressible potential flow equation (Laplace equation), subject to the no-penetration boundary condition at the solid surface,

$$\nabla(\Phi_0 + \phi) \cdot \mathbf{n} = 0, \quad (1)$$

where Φ_0 is the velocity potential of the incoming flow, ϕ is the perturbation velocity potential due to the wing, and \mathbf{n} is the normal vector at the solid surface.

Figure 12 shows an illustrative mesh setup for the flat plate and sawtooth serratation in the VLM. For illustrative purposes, the

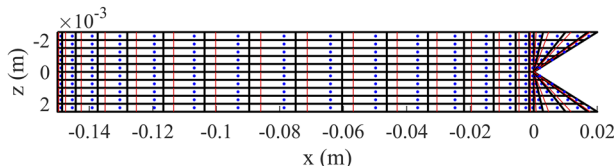


FIG. 12. An illustrative mesh setup in the VLM. The quadrilateral panels are enclosed by thick black lines. The leading edge segment of the horseshoe vortex element is shown by thin red lines. The collocation points are represented by blue dots.

mesh density is lower than that used for calculation, which has a mesh number of 50 (streamwise) \times 80 (spanwise). The surface is discretized into quadrilateral panels (thick black lines). A lumped horseshoe vortex is placed in each cell, whose spanwise segment (thin red line) is located at the quarter chord line of the panel and streamwise segments (not shown in the figure) extend to infinity along the streamwise direction. The collocation point (blue dot), where the boundary condition is enforced, is placed at the center of the three-quarter chord line of the panel. Under this setup, the Kutta condition is approximately satisfied.³⁷

The strength of each horseshoe vortex element needs to be solved. The induced velocity $\mathbf{v}_{i,j}$ at the i -th collocation point by the j -th horseshoe vortex element with unit strength can be calculated using the Biot–Savart law. Because of the periodicity in the spanwise direction, we need to count the influence of an infinite series of the image of the j -th vortex element,

$$\mathbf{v}_{i,j} = \sum_{k=-N_k}^{N_k} \mathbf{v}_{i,j}^k, \quad (2)$$

where $\mathbf{v}_{i,j}^k$ is the induced velocity by the k -th image of the j -th vortex element and N_k is a large number. Then, the boundary condition at the i -th collocation point is

$$\left(\mathbf{U}_0 + \sum_{j=1}^N \Gamma_j \mathbf{v}_{i,j} \right) \cdot \mathbf{n}_i = 0, \quad (3)$$

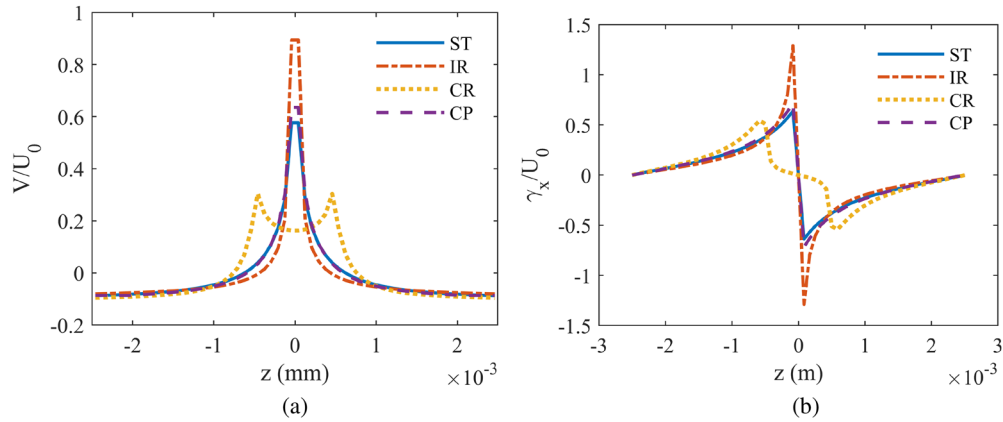


FIG. 13. (a) Crossflow velocity and (b) streamwise vortex density at one chord length downstream the trailing edge, acquired using the VLM. The flat plate is set at 0° AOA, and the serraion flap angle is 6°.

where N is the number of panels. The matrix

$$a_{i,j} = \mathbf{v}_{i,j} \cdot \mathbf{n}_i$$

typically has the aerodynamic influence coefficients, which is modified in this model due to the spanwise periodic condition. The distribution of vortex strength Γ_j can be acquired by solving the linear system. Other quantities, such as the crossflow velocity in the wake and the distribution of streamwise vorticity in the wake, can be calculated accordingly.

Before discussing the results, it needs to be pointed out that an exact quantitative agreement with the experiment is not expected for several reasons. First, since the size of the serrations is similar to the boundary layer thickness at the trailing edge, the local flow is expected to depend on the velocity field in the boundary layer, which cannot be captured by the potential method. Second, the viscous effect may play an important role near the serraion roots, where the physical dimensions are small. Last, the evolution of the streamwise vortex in the free space is not captured by the potential theory, which assumes semi-infinite horseshoe vortices. Nevertheless, as the driving force for the crossflow is the pressure difference across the serrations, which is mostly an inviscid phenomenon, this potential model can explain the qualitative performance of different serrated configurations.

Figure 13 shows the crossflow velocity and the density of the streamwise vortex at one chord length downstream the trailing edge, when the angle of attack is zero and the flap angle of the serraion is at 6°. The density of the streamwise vortex γ_x is defined as

$$\gamma_x = \frac{\Delta \Gamma_x}{\Delta z},$$

where Γ_x is the streamwise vortex acquired from superposing all the horseshoe vortex elements. γ_x/U_0 is a dimensionless quantity. From Fig. 13(a), it is clear that serrations lead to considerable crossflow downstream the serraion roots. The iron-shaped serrations give largest crossflow velocities at the center. The crossflow velocity of the ST and CP serrations is equal at most of the locations, except for those at the center, where the CP serrations give a slightly larger value. The CR serrations give relatively wider but weaker crossflow,

and the velocity profile shows two peaks downstream the endpoints of the flat part of the serration root. The crossflow is directly related to the counter-rotating streamwise vortex shown in Fig. 13(b). The streamwise vortex is mainly concentrated downstream the serration roots, rather than the serration tips. This is in accordance with the previous experimental study by Arce *et al.*³⁸ The iron-shaped serrat generates two strong counter-rotating vortices whose vortex cores are close to each other, which accounts for the strong crossflow. Although the chopped-root serrations have similar peak vortex strength to the sawtooth serrat, they generate relatively weaker crossflow since the vortices are far apart.

It has to be emphasized that due to the omission of the viscous effect in this VLM, the vortex strength is expected to be overpredicted. The reason is shown as follows. In the case of incompressible and isotropic fluids, the evolution of vorticity follows the vorticity transport equation

$$\frac{D\omega}{Dt} = (\omega \cdot \nabla) u + v \nabla^2 \omega. \quad (4)$$

The second term on the right-hand side of Eq. (4) represents the diffusion of vorticity due to the viscous effects, which is omitted in the VLM. However, it can be observed from Fig. 13(b) that the Laplacian of the streamwise vorticity (especially the term $\partial^2 \omega_x / \partial z^2$) is not small downstream the serrat root region. Therefore, the viscous diffusion should smooth out the vorticity distribution toward the downstream direction, which is the case observed in experiments.³⁸ The smoothing of the vorticity distribution will also reduce the peak crossflow velocity, which is over-estimated by the current inviscid VLM compared with the PIV measurement results in the study by León *et al.*¹³

Figure 14 shows the distribution of the same quantity as Fig. 13, but at a 6° angle of attack and zero flap angle. Here, the ranking of the crossflow velocities is the same. However, the magnitude of the crossflow velocity and the streamwise vortex intensity reduced to around one-third of those in Fig. 13. This means the generation of streamwise vortices and the corresponding crossflow is more sensitive to the flap angle than the angle of attack.

Similar findings have also been confirmed in the previous experimental study.¹³

In order to study the deformation of the serrations, we plot the product of the pressure coefficient C_p and the nondimensional moment arm $(x - x_{root})/(2h)$ in Fig. 15. The integration of this quantity across the serrat surface is proportional to the bending load acting on the serrat root. We can see that for a given angle attack and flap angle, the bending moment acting on the iron-shaped serrat is significantly larger than that on the sawtooth serrat. This explains why larger deformation was found for the iron-shaped serrations compared to the sawtooth serrations, despite their larger bending stiffness. In addition, it can be easily observed from Fig. 15 that the bending moment on the serrat is more sensitive to the flap angle rather than the angle of attack.

B. Comparison with analytical predictions on noise reduction

In this section, the analytical model by Lyu and Ayton¹ is used to predict the noise reduction by different trailing edge serrations. This model is a simplification based on Ayton's model,⁹ where Wiener–Hopf technique is used to acquire the exact scattering field generated by frozen turbulence past a semi-infinite flat plate with serrated trailing edges. Under the assumption that the serrat wavelength is less than half of the acoustic wavelength, the approximate expression for the nondimensional acoustic spectrum at a cylindrical coordinate (r, θ, z) is

$$\Psi(r, \theta, z) \sim \frac{\bar{k}}{2\pi r} \sin^2 \frac{\theta}{2} \frac{\bar{k}_1 + \bar{k}}{(\bar{k}_1 - \bar{k} \cos \theta)^2} \times \sum_{n=-\infty}^{\infty} \Pi_t(\omega, 2n\pi) |E_n(-\bar{k} \cos \theta)|^2. \quad (5)$$

Here, the reference scale for length, speed, and pressure is the serrat wavelength λ , the incoming flow speed U_0 , and twice the dynamic pressure ρU_0^2 , respectively. r is the radial distance from the observer and the trailing edge; θ is the observation angle with

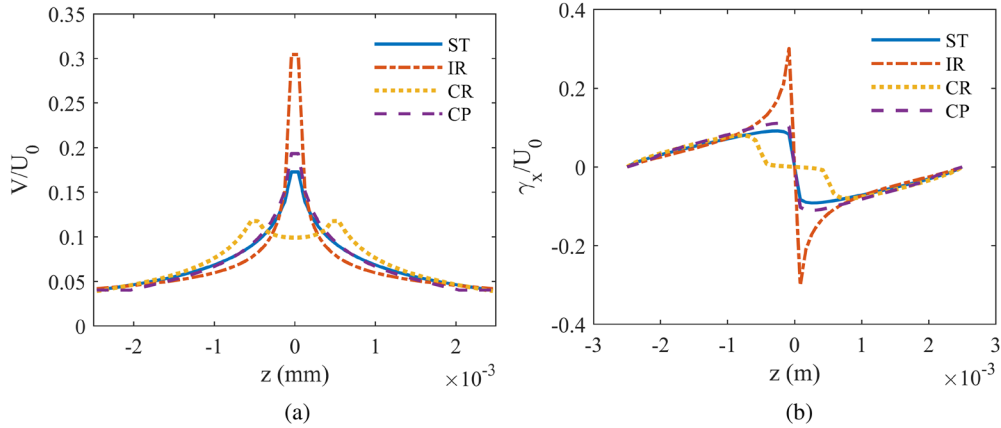


FIG. 14. (a) Crossflow velocity and (b) streamwise vortex density at one chord length downstream the trailing edge, acquired using the VLM. The flat plate is set at 6° AOA, and the serrat flap angle is 0° .

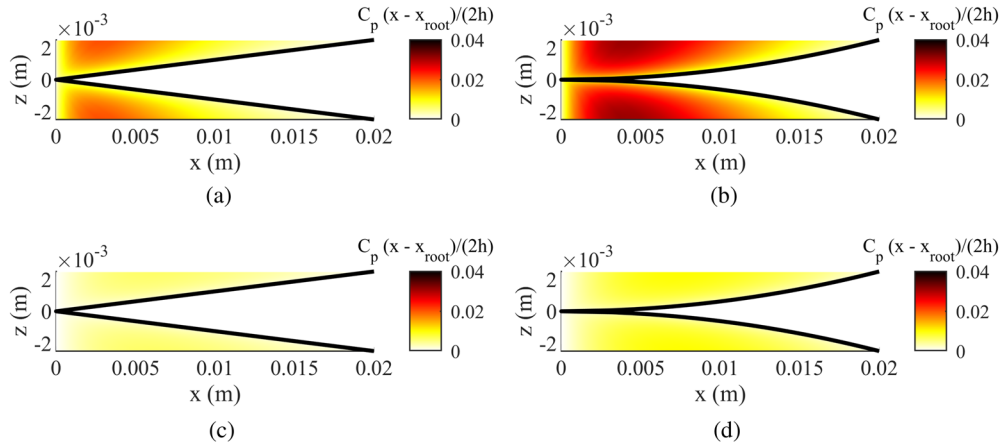


FIG. 15. Effective bending load $C_p(x - x_{root})/(2h)$ with respect to the serrat root in different configurations: (a) ST serrations, $AOA = 0^\circ$, $\delta_{flap} = 6^\circ$; (b) IR serrations, $AOA = 0^\circ$, $\delta_{flap} = 6^\circ$; (c) ST serrations, $AOA = 6^\circ$, $\delta_{flap} = 0^\circ$; (d) IR serrations, $AOA = 6^\circ$, $\delta_{flap} = 0^\circ$.

the downstream orientation defined as zero; $\bar{k} = k/\beta = k/\sqrt{1 - M^2}$ is the corrected non-dimensional acoustic wavelength, where M is the flow Mach number; k_1 is the non-dimensional hydrodynamic wavenumber, and $\bar{k}_1 = (k_1 + (kM - k_1 M^2))/\beta$ is the modified version; $\Pi_t(\omega, k_3)$ is the non-dimensional wavenumber frequency spectrum beneath the turbulent boundary layer just upstream the trailing edge. $E_n(-\bar{k} \cos \theta)$ is the only term that is related to the serrat geometry,

$$E_n(-\bar{k} \cos \theta) = \int_0^1 e^{i(\bar{k}_1 - \bar{k} \cos \theta)\bar{h}F(\eta)} e^{-i2n\pi\eta} d\eta, \quad (6)$$

where $\bar{h} = h/\beta$, in which h is the serrat amplitude, and $F(\eta)$ is the shape function of the serrat, which has a value between -1 and 1. Chase's model³⁹ was used to estimate the wavenumber-frequency spectrum of the wall pressure fluctuation, which is required as an

input to the scattering model. The non-dimensional expression is

$$\Pi_t(\omega, k_3) = \frac{4C_m \nu^{*4} \delta^4 k_1^2}{\alpha_c [(k_1^2 + k_3^2) \delta^2 + \chi^2]^2}, \quad (7)$$

where $C_m \approx 0.1533$, $\nu^* \approx 0.03$, $\chi \approx 1.33$, $\alpha_c \approx 0.7$ is the ratio between the convection velocity and the free-stream velocity, and δ is the non-dimensional boundary layer thickness. Here, we consider the case when the inflow velocity is at 20 m/s and the corresponding δ is 0.85. The observation angle θ is set at $\pi/2$ in the current study.

Figure 16(a) shows the predicted non-dimensional far-field noise spectra for the baseline and serrated configurations at $U_0 = 20$ m/s, and Fig. 16(b) gives the corresponding noise reduction. Here, the convention is to use a negative ΔSPL to represent noise reduction, and vice versa. The dimensional frequency is used for the horizontal axes to enable an easier comparison with the experiment.

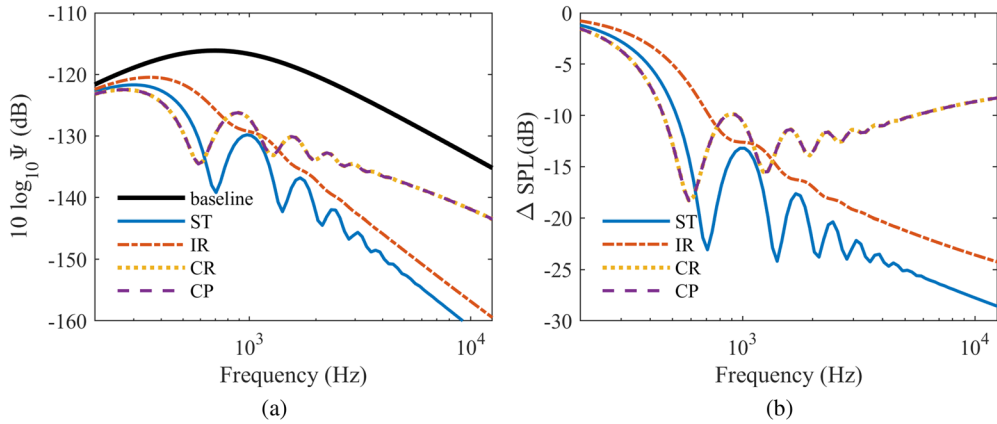


FIG. 16. (a) Predicted non-dimensional far-field noise and (b) corresponding noise reduction by different serrations according to the model by Lyu and Ayton.¹ $U_0 = 20$ m/s. A negative ΔSPL denotes noise reduction.

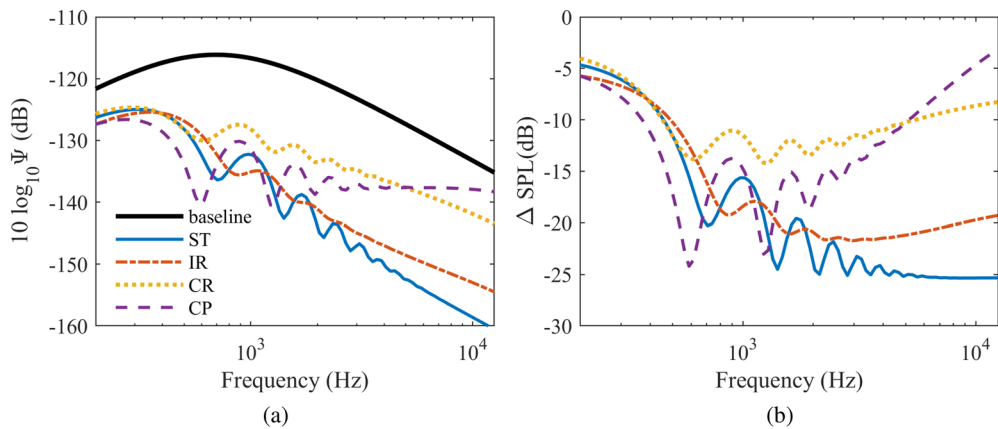


FIG. 17. (a) Predicted non-dimensional far-field noise and (b) corresponding noise reduction by different serrations according to the model by Lyu and Ayton,¹ with the modified formulation in Eqs. (8) and (9). $U_0 = 20$ m/s.

It is apparent that the analytical model considerably overestimates the noise reduction capability by serrations, which is only measured to be several decibels (see Fig. 5). The deviation is likely due to the assumption of the frozen turbulence in the model. In reality, this assumption is violated in two aspects. First, the amplitude of the wall pressure spectrum varies along the serrations.^{18,34} The low-frequency components decrease along the serration downstream, but the high-frequency component increases. Second, with the evolution of the turbulent structures along the serrations, the coherence of the wall pressure fluctuation between different streamwise directions is expected to be less than one. The decoherence is likely to reduce the efficacy of destructive interference. The second effect is expected to be more prominent at high frequencies, where the streamwise length scale of the turbulent structures becomes small compared to the length of serrations.

In Fig. 16(a), the predicted noise spectra for the CR and CP configurations are identical. This is because the factor $|E_n(-\bar{k} \cos \theta)|^2$ in Eq. (5) is invariant if the serrat geometry is mirrored with respect to the trailing edge. This identity deviates a lot from the experimental observations shown in Fig. 4, where the CR serrations perform significantly worse than the CP serrations at low frequencies. The deviation clearly demonstrates the limitation of the frozen turbulence assumption.

Here, we evaluate the effect of a streamwise-varying magnitude of the wall pressure fluctuation on the predicted noise reduction, which is a special case with a non-frozen turbulence assumption. For simplicity, we assume the decay/growth of the magnitude is exponential. This is a qualitative approach to highlight the physical mechanisms as the practical evolution of the wall pressure spectra are currently unknown. A similar empirical approach was adopted by Gershfeld⁴⁰ to account for the frequency-dependent reduction of airfoil leading edge noise by thickness. An equivalent imaginary part can be added to \bar{k}_1 when evaluating Eq. (6), i.e.,

$$E_n(-\bar{k} \cos \theta) = \int_0^1 e^{i(\bar{k}_1 - \bar{k} \cos \theta)\bar{h}F(\eta)} e^{-i2n\pi\eta} e^{\varepsilon(\bar{k}_1)(F(\eta)+1)\bar{h}} d\eta, \quad (8)$$

where $\varepsilon(\bar{k}_1)$ is a frequency-dependent growth/decay factor. The last term inside the integral is equal to one at the root of the serrations.

Although the wall pressure spectra along the serrat are not available in the current study, we may infer the general trend from the numerical study by Avallone, van der Velden, and Ragni.¹⁸ In their study, the wall pressure spectral level reduces along the streamwise direction if $St_\delta \lesssim 1$; in the low-frequency end, the root-to-tip reduction is around 8 dB, while, at $St_\delta = 1.7$, the root-to-tip increment is around 4 dB. In the current experimental study, at $U_0 = 20$ m/s, the frequency corresponding to $St_\delta = 1$ is ~ 4700 Hz. Thus, we assume

$$\varepsilon(\bar{k}_1) = -0.23 + 0.46 \exp\left(-\frac{\bar{k}_1}{\bar{k}_{1,cr}} \ln 2\right), \quad (9)$$

where $\bar{k}_{1,cr} = 10.7$ is the value of \bar{k}_1 corresponding to $St_\delta = 1$, in which case $\varepsilon(\bar{k}_1) = 0$. In this formulation, the root-to-tip reduction of the wall pressure spectral magnitude is 8 dB at $\bar{k}_1 = 0$ and -8 dB when \bar{k}_1 is very large.

In Fig. 17, we can see that below 2 kHz, the noise reduction by the CP configuration is similar to that by the ST configuration and is considerably better than that by the CR configuration. At frequencies above 5 kHz, the CR serrations start to outperform the CP serrations in terms of noise reduction. Thus, the predictions are qualitatively more consistent with the experimental observations [see Fig. 4(a)] compared to predictions using the frozen turbulence assumption [Fig. 16(a)]. A quantitative prediction of ΔSPL is not achieved. Nevertheless, the purpose of the above analysis is to emphasize the necessity of considering the variation of the wall pressure spectral magnitude along the serrations.

V. CONCLUSIONS

This paper presents a comprehensive study on the effect of serrat geometry and flexibility on trailing edge noise. It is observed that with the same serrat wavelength λ and root-to-tip distance $2h$, the serrat geometry can affect the noise spectrum

significantly. The flexible serrations can give an extra reduction in the high-frequency range for certain serrat geometry. However, when the serrations are too flexible, above a critical flow speed, they can undergo flutter instability, which leads to significant tonal and broadband noise generation. Thus, the selection of the flexibility of the serrations should depend on the working conditions to ensure the stability of the serrations. Deformation and force measurement results show that the flexible serrations are able to align better with the flow and reduce the aerodynamic loading on the airfoil. The deformation depends not only on the serrat stiffness and flow speed but also on the aerodynamic loading for the serrat, which is dependent on the serrat geometry. With carefully designed flexibility, the flexible serrat is expected to give the benefit that the noise reduction performance is less sensitive to the installation error (i.e., non-zero flap angle) or variation in the working condition (angle of attack).

A modified vortex lattice method (VLM) is used to compute the flow structure around different serrations. It shows that when the serrations have a non-zero flap angle, or when the airfoil is at an angle of attack, strong crossflow and counter-rotating streamwise vortices can occur downstream the serrat root. The crossflow intensity is more sensitive to the serrat flap angle compared to the angle of attack of the airfoil. This observation is in accordance with previous experimental studies. In addition, the model qualitatively shows that the iron-shaped serrations lead to a more intense vortex structure and stronger crossflow, which agrees with the intense high-frequency noise generated by the iron-shaped serrations observed in the experiment. The model also predicts a higher bending loading for the iron-shaped serrations compared to the sawtooth condition, which agrees with the deformation and the lift measurement. However, due to the omission of the viscous effect, the vortex intensity and crossflow intensity are over-estimated. Last, the recent analytical model by Lyu and Ayton¹ is considered to predict the effect of serrat geometry on trailing edge noise. The qualitative and quantitative deviation from experimental results clearly indicates the limitation of adopting the frozen turbulence assumption. A modified model that includes the growth/decay in the turbulent wall pressure fluctuation along the serrat shows a better qualitative agreement with the experimental observation. Nevertheless, there is still a large room to improve the accuracy of the noise prediction model for trailing edge serrations, and the development of boundary layers along the serrations should be included in the noise prediction model before it can be applied for optimization purposes.

ACKNOWLEDGMENTS

P.Z. would like to thank the Hong Kong RGC Ph.D. Fellowship (Ref. No. PF16-01286) for supporting part of the Ph.D. thesis research. Y.F. would like to thank the support of the Hong Kong Innovation and Technology Commission (Grant No. ITS/387/17FP). This work was performed at the Aerodynamics Acoustics & Noise control Technology Centre (aantc.ust.hk).

DATA AVAILABILITY

The data that support the findings of this study are available from the corresponding author upon reasonable request.

REFERENCES

- ¹B. Lyu and L. J. Ayton, "Rapid noise prediction models for serrated leading and trailing edges," *J. Sound Vib.* **469**, 115136 (2020).
- ²D. P. Lockard and G. M. Lilley, "The airframe noise reduction challenge," Technical Report No. NASA-TM-2004-213013, 2004.
- ³S. Oerlemans, M. Fisher, T. Maeder, and K. Kögler, "Reduction of wind turbine noise using optimized airfoils and trailing-edge serrations," *AIAA J.* **47**, 1470–1481 (2009).
- ⁴T. F. Brooks, D. S. Pope, and M. A. Marcolini, "Airfoil self-noise and prediction," Technical Report No. NASA-RP-1218, 1989.
- ⁵J. E. Ffowcs Williams and L. H. Hall, "Aerodynamic sound generation by turbulent flow in the vicinity of a scattering half plane," *J. Fluid Mech.* **40**, 657–670 (1970).
- ⁶R. K. Amiet, "Noise due to turbulent flow past a trailing edge," *J. Sound Vib.* **47**, 387–393 (1976).
- ⁷M. S. Howe, "Noise produced by a sawtooth trailing edge," *J. Acoust. Soc. Am.* **90**, 482–487 (1991).
- ⁸B. Lyu, M. Azarpeyvand, and S. Sinayoko, "Prediction of noise from serrated trailing edges," *J. Fluid Mech.* **793**, 556–588 (2016).
- ⁹L. J. Ayton, "Analytic solution for aerodynamic noise generated by plates with spanwise-varying trailing edges," *J. Fluid Mech.* **849**, 448–466 (2018).
- ¹⁰M. Gruber, "Airfoil noise reduction by edge treatments," Ph.D. thesis, University of Southampton, 2012.
- ¹¹D. J. Moreau and C. J. Doolan, "Noise-reduction mechanism of a flat-plate serrated trailing edge," *AIAA J.* **51**, 2513–2522 (2013).
- ¹²A. Vathylakis, C. C. Paruchuri, T. P. Chong, and P. Joseph, "Sensitivity of airfoil self-noise reductions to serrat flap angles," AIAA Paper No. 2016-2837, 2016.
- ¹³C. A. León, D. Ragni, S. Pröbsting, F. Scarano, and J. Madsen, "Flow topology and acoustic emissions of trailing edge serrations at incidence," *Exp. Fluids* **57**, 91 (2016).
- ¹⁴C. A. León, R. Merino-Martínez, D. Ragni, F. Avallone, F. Scarano, S. Pröbsting, M. Snellen, D. G. Simons, and J. Madsen, "Effect of trailing edge serrat-flow misalignment on airfoil noise emissions," *J. Sound Vib.* **405**, 19–33 (2017).
- ¹⁵T. P. Chong, P. F. Joseph, and M. Gruber, "Airfoil self noise reduction by non-flat plate type trailing edge serrations," *Appl. Acoust.* **74**, 607–613 (2013).
- ¹⁶T. P. Chong and E. Dubois, "Optimization of the poro-serrated trailing edges for airfoil broadband noise reduction," *J. Acoust. Soc. Am.* **140**, 1361–1373 (2016).
- ¹⁷F. Avallone, W. C. P. van der Velden, D. Ragni, and D. Casalino, "Noise reduction mechanisms of sawtooth and combed-sawtooth trailing-edge serrations," *J. Fluid Mech.* **848**, 560–591 (2018).
- ¹⁸F. Avallone, W. C. P. van der Velden, and D. Ragni, "Benefits of curved serrations on broadband trailing-edge noise reduction," *J. Sound Vib.* **400**, 167–177 (2017).
- ¹⁹C. A. León, R. Merino-Martínez, D. Ragni, F. Avallone, and M. Snellen, "Boundary layer characterization and acoustic measurements of flow-aligned trailing edge serrations," *Exp. Fluids* **57**, 182 (2016).
- ²⁰M. Gruber, P. Joseph, and T. P. Chong, "Experimental investigation of airfoil self noise and turbulent wake reduction by the use of trailing edge serrations," AIAA Paper No. 2010-3803, 2010.
- ²¹F. Avallone, S. Pröbsting, and D. Ragni, "Three-dimensional flow field over a trailing-edge serrat and implications on broadband noise," *Phys. Fluids* **28**, 117101 (2016).
- ²²T. Bachmann, S. Klán, W. Baumgartner, M. Klaas, W. Schröder, and H. Wagner, "Morphometric characterisation of wing feathers of the barn owl *Tyto alba pratincola* and the pigeon *Columba livia*," *Front. Zool.* **4**, 23 (2007).
- ²³D. G. Crighton and F. G. Leppington, "Scattering of aerodynamic noise by a semi-infinite compliant plate," *J. Fluid Mech.* **43**, 721–736 (1970).
- ²⁴J. W. Jaworski and N. Peake, "Aerodynamic noise from a poroelastic edge with implications for the silent flight of owls," *J. Fluid Mech.* **723**, 456–479 (2013).
- ²⁵M. Herr and W. Dobrznyski, "Experimental investigations in low-noise trailing edge design," *AIAA J.* **43**, 1167–1175 (2005).
- ²⁶M. Herr, "Design criteria for low-noise trailing-edges," AIAA Paper No. 2007-3470, 2007.

- ²⁷A. Finez, M. Jacob, E. Jondeau, and M. Roger, "Broadband noise reduction with trailing edge brushes," AIAA Paper No. 2010-3980, 2010.
- ²⁸E. Talboys, T. F. Geyer, and C. Brücker, "An aeroacoustic investigation into the effect of self-oscillating trailing edge flaplets," *J. Fluids Struct.* **91**, 102598 (2019).
- ²⁹T. Zhou, Y. Sun, R. Fattah, X. Zhang, and X. Huang, "An experimental study of trailing edge noise from a pitching airfoil," *J. Acoust. Soc. Am.* **145**, 2009–2021 (2019).
- ³⁰H. Bu, X. Huang, and X. Zhang, "A compressive-sensing-based method for radial mode analysis of aeroengine fan noise," *J. Sound Vib.* **464**, 114930 (2020).
- ³¹M. Drela, "XFOIL: An analysis and design system for low Reynolds number airfoils," in *Low Reynolds Number Aerodynamics* (Springer, 1989), pp. 1–12.
- ³²P. Zhou, G. N. Lui, and X. Zhang, "An experimental investigation of the effect of owl-inspired velvety coating on trailing edge noise," AIAA Paper No. 2019-2622, 2019.
- ³³B. Lyu and L. J. Ayton, "Serrated leading-edge and trailing-edge noise prediction models for realistic wavenumber frequency spectra," AIAA Paper No. 2019-2674, 2019.
- ³⁴D. Ragni, F. Avallone, W. C. P. van der Velden, and D. Casalino, "Measurements of near-wall pressure fluctuations for trailing-edge serrations and slits," *Exp. Fluids* **60**, 6 (2019).
- ³⁵C. Eloy, C. Souilliez, and L. Schouveiler, "Flutter of a rectangular plate," *J. Fluids Struct.* **23**, 904–919 (2007).
- ³⁶C. Eloy, R. Lagrange, C. Souilliez, and L. Schouveiler, "Aeroelastic instability of cantilevered flexible plates in uniform flow," *J. Fluid Mech.* **611**, 97–106 (2008).
- ³⁷J. Katz and A. Plotkin, *Low-speed Aerodynamics* (Cambridge University Press, 2001), Vol. 13.
- ³⁸C. Arce, D. Ragni, S. Pröbsting, and F. Scarano, "Flow field around a serrated trailing edge at incidence," AIAA Paper No. 2015-0991, 2015.
- ³⁹D. M. Chase, "The character of the turbulent wall pressure spectrum at subconvective wavenumbers and a suggested comprehensive model," *J. Sound Vib.* **112**, 125–147 (1987).
- ⁴⁰J. Gershfeld, "Leading edge noise from thick foils in turbulent flows," *J. Acoustical Soc. Am.* **116**, 1416–1426 (2004).